POLITECNICO DI TORINO
SORBONNE UNIVERSITÉ

Double Master Degree in Physics of Complex Systems

Tesi di Laurea Magistrale

Chemotaxis in high dimensional bacterial mixtures

Relatori
Prof. Julien Tailleur
Prof. Andrea Pagnani

Candidata
Sofia Marchioretto

Luglio 2025

Politecnico di Torino

SCIENCES SORBONNE UNIVERSITÉ

Abstract

Active matter systems, composed of self-propelled agents that continuously consume energy, exhibit rich non-equilibrium behavior and complex spatial organization. A key challenge is understanding how local interactions that regulate motility give rise to emergent structures, particularly in multi-species systems where ecological diversity plays a role. In this work, we investigate the role of chemotaxis—a form of motility control based on chemical gradients—in driving self-organization in dry scalar active matter. Focusing on systems with fixed population size, we show that weak, random chemotactic couplings between species can generate spatial patterns even in the absence of systematic interactions. Using a combination of theoretical analysis and numerical simulations, we first study the dynamics of a single-species system, then extend our approach to active mixtures. Our results highlight a novel mechanism for pattern formation in active matter and offer insights relevant to biological and ecological systems.

Table of contents

Chapter 1

Introduction

Active matter refers to a kind of soft matter composed of individual agents, *i.e.* active particles, that consume environmental or internal energy to move or produce mechanical work. This paradigm clearly draws inspiration from living matter, in which activity is ubiquitous at all scales, ranging from the walk of pedestrians down to bacteria swimming in liquid via rotating flagella, and is also relevant for non-living imitations, such as synthetic microswimmers. The defining feature of active matter is that energy injection happens at the microscopic scale of each individual agent, keeping the whole system perpetually out of equilibrium, in contrast with what happens to usual passive systems, which relax toward thermal equilibrium. Interactions between active agents lead to a variety of emergent collective behavior, including pattern formation, spontaneous flows, and large-scale organization. Understanding the rich phenomenology exhibited by active matter is not only a fundamental challenge in statistical physics but also of increasing importance for biology and material science. It offers insights into processes such as the organization of biological tissues, bacterial colony growth, and the design of smart, responsive materials. However, establishing a unified theoretical framework remains a difficult task, as the intrinsic non-equilibrium nature of the problem prevents the use of conventional statistical mechanics to describe macroscopic behavior.

A central question in active matter research is how motile cells self-organize in space. This question is broadly relevant in biology, it applies for example to the early stages of embryonic development (morphogenesis) and to the formation of ecological communities in highly diverse ecosystems. The latter has been extensively studied in theoretical ecology, and while various pattern-formation mechanisms have been proposed—such as genetic drift, mutualistic interactions or competition for resources—relatively little attention has been paid to the regulation of motility, meaning the adaptation of motion in response to external factors. Yet, motility control is an intrinsic tool of nearly every living organism and has been proven to be a driver for the formation of macroscopic structure [3, 4, 9, 10].

We thus aim to investigate the role of motility regulation in shaping spatial assemblies of active particles. This is a challenging problem due to the inherently non-equilibrium behavior of such systems, which requires studying the collective dynamics over time while accounting for local interactions between particles. Moreover, we are particularly interested in high-dimensional systems involving many distinct species, as is often the case in natural ecosystems, as for example bacterial colonies. This further increases the complexity of the problem and calls for the use of statistical methods to capture the emergent

behavior.

Focusing mainly on the dynamics in space, we will consider timescales shorter than the ecological scales at which population dynamics starts to play a role. *Escherichia coli*, for example, divides approximately every 20 minutes, while its motion typically changes direction on a timescale of about 1 second [2]. This separation of timescales allows us to consider dynamics over times t much longer than the reorientation time, while assuming a constant population size. In particular, we will consider dry scalar active matter, where the term dry refers to the fact that the degrees of freedom of the environment surrounding the active particles are not taken into account, but rather integrated out, leading to the non-conservation of momentum in the system. The term scalar, instead, describes the symmetry broken by particle shapes: scalar particles can be visualized as spherical, while nematic ones model rod-like particles with a given angular anisotropy. Finally, if nematic particles break their head/tail symmetry and manifest a preferential direction of motion along their axis, we talk about polar active matter.

In this work, we focus on chemotaxis, that is a motility regulation based on the gradient of a chemical field mediating the interactions among particles. Specifically, we show that weak, random chemotactical interactions between species represent a new route to self-organization. Through theoretical work and numerical simulations, we demonstrate how this mechanism is able to generate spatial patterns in scalar active systems, even in the absence of pre-existing systematic interactions.

The report is organized as follows: in Section 2, we introduce the model and revise the mathematical tools that have been employed for the study of monodisperse systems, *i.e.*, comprising of one single strain. Section 3 presents the corresponding numerical simulations for the one-species system. In section 4 we extend the theoretical framework to active mixtures, meaning systems with multiple species of active particles. Finally, Section 5 concludes with a discussion of future directions.

Chapter 2

Motility regulation in monodisperse systems

2.1 Models of active particles

The mathematical modeling of active particles combines deterministic self-propelled motion with a stochastic mechanism for changing direction. The two most common models that implement this principle in opposite ways are Run-and-Tumble Particles (RTPs) and Active Brownian Particles (ABPs).

The RTP model describes particles that move with a self-propulsion speed v along a direction $\mathbf{u}$ during run phases, which are interspersed with tumbling phases when the particle randomly re-orients. Tumbles occur with a rate α and will be considered instantaneous events. A typical trajectory is represented in Figure 2.1. Including the possibility of diffusion with diffusion coefficient D_t, the dynamics of the position $\mathbf{r}$ of the particle in d spatial dimensions is given by:

$$\begin{aligned} &\dot{\mathbf{r}} = v\mathbf{u} + \sqrt{2D_t}\boldsymbol{\eta}(t) \qquad \text{with} \quad \langle \boldsymbol{\eta}(t) \rangle = 0 \quad \langle \boldsymbol{\eta}(t)\boldsymbol{\eta}(t') \rangle = \delta(t-t')\mathbb{I}_d \\ &\mathbf{u} \xrightarrow{\alpha} \mathbf{u}' \in \mathbb{S}^{d-1} \end{aligned} \tag{2.1}$$

where $\boldsymbol{\eta}$ is a delta-correlated Gaussian noise with zero mean and unit variance. Because of the discrete tumblings, the stochastic process cannot be written in terms of a Langevin equation, but one can find that the probability $\mathcal{P}(\mathbf{r}, \mathbf{u}, t)$ of the particle to be in position $\mathbf{r}$ with orientation $\mathbf{u}$ at time t obeys the following Master equation:

$$\partial_t \mathcal{P} = -\nabla_{\mathbf{r}} \cdot [v\mathbf{u}\mathcal{P} - D_t \nabla_{\mathbf{r}} \mathcal{P}] - \alpha \mathcal{P} + \frac{\alpha}{\Omega_{d-1}} \int_{\mathbf{S}^{d-1}} \mathcal{P}(\mathbf{r}, \mathbf{u}', t)\, d\mathbf{u}' \tag{2.2}$$

It is interesting to look at the dynamics of the unit vector $\mathbf{u}$, averaged over the stochasticity introduced by the tumblings and spatial diffusivity:

$$\frac{d\langle \mathbf{u} \rangle}{dt} = \int_{\mathbb{R}^d} d\mathbf{r} \int_{\mathbb{S}^{d-1}} d\mathbf{u}\, \mathbf{u}\, \partial_t \mathcal{P}(\mathbf{r}, \mathbf{u}', t) = -\frac{1}{\tau}\langle \mathbf{u} \rangle \qquad \Rightarrow \qquad \langle \mathbf{u}(t) \rangle = e^{-\alpha t}\langle \mathbf{u}(0) \rangle \tag{2.3}$$

One finds that the average direction of the motion decorrelates exponentially fast over a time scale called persistence time τ. For RTP motion, it clearly corresponds to the typical time interval between tumbles $\tau = \frac{1}{\alpha}$. The persistence length is the typical distance covered during τ: $l_p = \frac{v}{\alpha}$.

In contrast, the ABP model features a biologically more realistic continuous diffusion of the orientation vector $\mathbf{u}$ in the unit sphere $\mathbb{S}^{d-1}$ with a diffusion coefficient Γ. The motion is schematically depicted in Figure 2.1. For simplicity we present the corresponding dynamical equations in two dimensions where $\mathbf{u}$ is identified by one angle θ:

$$\begin{aligned} \dot{\mathbf{r}} &= v\mathbf{u} + \sqrt{2D_t}\boldsymbol{\eta}(t) \\ \dot{\theta} &= \sqrt{2\Gamma}\xi(t) \end{aligned} \tag{2.4}$$

where $\boldsymbol{\eta}$ and ξ are standard white Gaussian noises. Since the motion of both $\mathbf{r}$ and $\mathbf{u}$ is continuous, the corresponding Master equation is a multivariate Fokker-Planck equation:

$$\partial_t \mathcal{P} = -\nabla_{\mathbf{r}} \cdot [v\mathbf{u}\mathcal{P} - D_t \nabla_{\mathbf{r}} \mathcal{P}] + \nabla^2_{\mathbf{u}}(\Gamma\mathcal{P}) \tag{2.5}$$

Analogously, one can see that the average orientation vector again decorrelates exponentially over time, with persistence time $\tau = \frac{1}{(d-1)\Gamma}$. The persistence length is therefore $l_p = \frac{v}{(d-1)\Gamma}$.

As a side comment, we note that for typical organisms spatial diffusion of agents driven by thermal noise can often be neglected. For instance, the friction coefficient γ of *Escherichia Coli* can be expressed by Stokes's law (since its Reynolds number is much smaller than unity), allowing us to quantify the displacement due to noise during the interval τ:

$$l_{\text{diff}} = \sqrt{D_t \tau} = \sqrt{\frac{k_B T}{\gamma}\tau} = \sqrt{\frac{k_B T}{6\pi\eta r}\tau} \approx 10^{-7}\ \text{m} \tag{2.6}$$

during the same time interval, the bacterium has traveled a distance equal to the persistence length, which can be estimated by data in [2] and is roughly $l_p \approx 10^{-5}$ m. Being $l_p \gg l_{\text{diff}}$, D_t can usually be neglected.

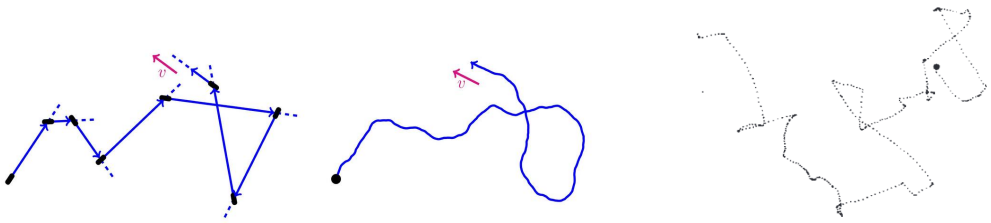

Figure 2.1: Typical trajectories of a Run-and-Tumble particle (RTP) on the left, and of an Active Brownian particle (ABP) in the center. Image taken from [12]. 2d projection of a tridimensional measured trajectory of a wild-type *E. Coli* bacterium. Image taken from [2].

2.2 Motility regulation

A widespread strategy in biological or synthetic systems is the spatial and temporal modulation of the motility parameters v, α, Γ. For example, many motile organisms can steer their motion in search of food or to escape from threats, or adjust their speed in response to local crowding. The regulation can come either from some external factor or due to interactions among particles, we model both these mechanisms via a controlling field $c(\mathbf{r}, t)$ that is either externally imposed in the former case, or produced by the particles themselves in the latter. Therefore:

$$\begin{aligned} v &= v_0(c(\mathbf{r},t)) - v_1 \mathbf{u} \cdot \nabla_{\mathbf{r}} c(\mathbf{r},t) \\ \alpha &= \alpha_0(c(\mathbf{r},t)) + \alpha_1 \mathbf{u} \cdot \nabla_{\mathbf{r}} c(\mathbf{r},t) \\ \Gamma &= \Gamma_0(c(\mathbf{r},t)) + \Gamma_1 \mathbf{u} \cdot \nabla_{\mathbf{r}} c(\mathbf{r},t) \end{aligned} \tag{2.7}$$

When the particles react at the local value of the field, as in the first terms of the equations, we refer to the regulation as kinesis, when instead the gradient of the field is involved, as in the second terms of the equations, regulation is called taxis. In the context of this thesis, c will represent the concentration of a chemical field produced by the particles, therefore, we will speak about quorum sensing in the first case and chemotaxis in the second. Finally, we note that positive values for v_1, α_1, Γ_1 model particles attracted to the chemical c, repelled otherwise.

2.3 Dynamics of chemical fields

In our model, interactions are mediated by a chemical field present in the environment with concentration $c(\mathbf{r}, t)$: after being produced by particles, it can travel and be detected by other particles. A simple model for its dynamics is:

$$\partial_t c(\mathbf{r},t) = \beta \rho(\mathbf{r},t) + D_c \nabla^2 c(\mathbf{r},t) - \chi c(\mathbf{r},t) \tag{2.8}$$

where ρ is the local density of particles. Equation 2.8 expresses the fact that the chemical is produced by each of them with rate β, then diffuses in space with diffusivity D_c, and degrades with a constant rate χ.
Since particle number is fixed, ρ is a locally conserved field and therefore varies on timescales $\mathcal{O}(L^\alpha)$ with L system size and $\alpha > 1$ which depends on the specific type of dynamics (for instance, $\alpha = 2$ for diffusion, $\alpha = 1$ for ballistic motion). Due to the linear degradation term in equation 2.8, the relaxation of the chemical field is instead much faster, happening on timescales $1/\chi \sim \mathcal{O}(1)$. Being interested in the motion of particles, we can then consider c to adapt adiabatically to ρ, and set $\partial_t c = 0$. Therefore:

$$\mathcal{L} c(\mathbf{r},t) \equiv \frac{1}{\beta}\left(\chi - D_c \nabla^2\right) c(\mathbf{r},t) = \rho(\mathbf{r},t) \tag{2.9}$$

$$\Rightarrow \quad c(\mathbf{r},t) = (G * \rho(t))(\mathbf{r}) = \int d\tilde{\mathbf{r}}\, G(\mathbf{r} - \tilde{\mathbf{r}}) \rho(\tilde{\mathbf{r}}, t) \tag{2.10}$$

where G is the Green function associated to the linear operator $\mathcal{L}$, defined such that $\mathcal{L} G(\mathbf{r}) = \delta(\mathbf{r})$. We report the Green functions in one and two spatial dimensions, along

with their Fourier transform which will be useful in the following chapters. Defining a characteristic length $l = \sqrt{D_c/\chi}$, one finds in one dimensional space:

$$G(x) = \frac{\beta l}{2D_c} e^{-\frac{|x|}{l}} \qquad \Rightarrow \qquad \hat{G}(q) = \int_{\mathbb{R}} dx\ e^{-iqr} G(x) = \frac{\beta l^2}{D_c} \frac{1}{1+(lq)^2} \tag{2.11}$$

while in two dimensions:

$$G(\mathbf{r}) = \frac{\beta}{2\pi D_c} K_0\left(\frac{|\mathbf{r}|}{l}\right) \qquad \Rightarrow \qquad \hat{G}(\mathbf{q}) = \int_{\mathbb{R}^2} d\mathbf{r}\ e^{-i\mathbf{q}\cdot\mathbf{r}} G(\mathbf{r}) = \frac{\beta l^2}{D_c} \frac{1}{1+(l|\mathbf{q}|)^2} \tag{2.12}$$

where K_0 is the 0^{th} order modified Bessel function of the second kind. A derivation of its bidimensional Fourier transform can be found in the Appendices 6.1. We note that the chemical field can possibly obey more complicated dynamics, alternative to 2.8, in such cases the time separation argument remains valid and $c(\mathbf{r}, t)$ is again a linear functional of the density ρ convoluted with a general kernel $K(\mathbf{r})$:

$$c(\mathbf{r}, t) = (K * \rho(t))(\mathbf{r}) \tag{2.13}$$

2.4 Motility regulation as a pathway for self-organization

Motility regulation is a fundamental ingredient in the emergence of self-organization in motile systems. By self-organization, we refer to the spontaneous formation of ordered structures or dynamical patterns from initially disordered states, driven solely by local interactions without the need for external coordination. In active matter systems—ranging from bacterial colonies to synthetic microswimmers—spatial or temporal modulation of motility parameters such as speed, tumbling rate, or rotational diffusivity enables complex collective behaviors like clustering, band formation, and patterning. Experimentally, several studies have demonstrated that controlling motility can induce such phenomena. For example, in bacterial populations, the secretion of signaling molecules that modulate motility has been shown to lead to high-density aggregates via quorum sensing [3] or chemotactic [10] mechanisms. As a prime example of a synthetic system, light-activated Janus colloids exhibit clustering and phase separation when their propulsion speed is controlled by a spatially inhomogeneous light field [4, 9]. Even in macroscopic systems, such as flocks of birds or schools of fish, mutual interactions, effectively modulating directional persistence and speed based on the presence of neighbors, can result in coherent motion. In all these cases, motility regulation acts as a feedback mechanism linking individual behavior to the evolving environment. Among the many collective behaviors driven by motility regulation, special emphasis in this report will be placed on motility-induced phase separation (MIPS), that is the macroscopic separation of active matter in liquid and gas phases, even in the absence of attractive microscopic interactions. We now report from [12] a heuristic argument explaining the origin of such phenomenon. For simplicity we consider active particles without translational diffusivity. Starting from the equations of motion 2.1 or 2.4, one finds that the probability of one of them to be at position $\mathbf{r}$ with velocity oriented in direction $\mathbf{u}$ obeys the master equation:

$$\partial_t P(\mathbf{r}, \mathbf{u}, t) = -\nabla \cdot [v(\mathbf{r})\mathbf{u}P(\mathbf{r}, \mathbf{u}, t)] + \Theta P(\mathbf{r}, \mathbf{u}, t) \tag{2.14}$$

where the linear operator Θ accounts for the angular dynamics. Assuming a fixed velocity field $v(\mathbf{r})$, for both RTPs and ABPs, the steady-state solution of equation 2.14 is:

$$P_{ss}(\mathbf{r}, \mathbf{u}) = \frac{\kappa}{v(\mathbf{r})} \tag{2.15}$$

with κ a normalizing constant. This tells us that active particles tend to concentrate in regions where they move slower. Then, if interactions are such to slow down particles in high-density regions, this closes a positive feedback loop in which dense areas become denser and denser, triggering phase separation. We can derive a quantitative criterion for the onset of instability by considering active particles with local self-propulsion speed $v(\rho(\mathbf{r}))$ modulated by quorum-sensing interactions. Upon perturbing a uniform density profile ρ_0, $\rho(\mathbf{r}) = \rho_0 + \delta\rho(\mathbf{r})$, the velocity field gets modified, to linear order, to:

$$v(\rho(\mathbf{r})) = v(\rho_0) + \delta\rho(\mathbf{r})v'(\rho_0) \tag{2.16}$$

where $v' \equiv \frac{dv}{d\rho}$. In turns, the density field tends to relax towards its steady state:

$$\rho(\mathbf{r}) = \frac{\tilde{\kappa}}{v(\rho(\mathbf{r}))} = \frac{\tilde{\kappa}}{v(\rho_0)}\left(1 - \frac{v'(\rho_0)}{v(\rho_0)}\delta\rho\right) + \mathcal{O}(\delta\rho^2) \tag{2.17}$$

The mass conservation condition $\int d\mathbf{r}\ \delta\rho(\mathbf{r}) = 0$ fixes the normalization constant to $\tilde{\kappa} = \rho_0 v(\rho_0)$. Equation 2.17 can then be expressed in terms of a new perturbation $\delta\tilde{\rho}$:

$$\rho(\mathbf{r}) \equiv \rho_0 + \delta\tilde{\rho} \qquad \text{with} \qquad \delta\tilde{\rho} = -\rho_0 \frac{v'(\rho_0)}{v(\rho_0)}\delta\rho. \tag{2.18}$$

This shows that the initial perturbation grows, *i.e.*, $\delta\tilde{\rho} > \delta\rho$ if $v(\rho)$ decreases fast enough, specifically when

$$\frac{v'(\rho_0)}{v(\rho_0)} < -\frac{1}{\rho_0} \quad \Leftrightarrow \quad \frac{d}{d\rho}\left[\rho v(\rho)\right]\Big|_{\rho_0} < 0. \tag{2.19}$$

Remarkably, the same instability condition will be derived from more rigorous argument in section 2.7.

2.5 From micro to macro

Equations 2.1-2.4 express the microscopic stochastic laws of motion of particles. In a statistical mechanics spirit, we are interested in coarse graining such a dynamics to obtain, possibly, some Thermodynamics rules governing active matter. In this section we will outline the methods that have previously been developed in [7] to construct a macroscopic effective dynamics for the spatial density of particles $\rho(\mathbf{r}, t)$.

Making an effort to keep the most general setting possible, we will allow for both instantaneous tumblings and continuous diffusion of the orientation vector $\mathbf{u}$. Moreover we will consider smoothly varying motility regulation given by equations 2.7. The master equation for the probability $\mathcal{P} \equiv \mathcal{P}(\mathbf{r}, \mathbf{u}, t)$ of a given particle to be found at time t in position $\mathbf{r}$ with orientation $\mathbf{u}$ is then:

$$\partial_t \mathcal{P} = -\nabla_{\mathbf{r}} \cdot [v\mathbf{u}\mathcal{P} - D_t \nabla_{\mathbf{r}} \mathcal{P}] - \alpha \mathcal{P} + \frac{1}{\Omega_{d-1}} \int_{\mathbf{S}^{d-1}} \alpha(\mathbf{u}') \mathcal{P}(\mathbf{r}, \mathbf{u}', t)\, d\mathbf{u}' + \nabla^2_{\mathbf{u}}(\Gamma \mathcal{P}) \quad (2.20)$$

where Ω_d is the solid angle in d dimesions. The first step is integrating out the angular dependence on $\mathbf{u}$ to obtain a closed equation for $p(\mathbf{r}, t) = \int_{\mathbf{S}^{d-1}} d\mathbf{u}\ \mathcal{P}(\mathbf{r}, \mathbf{u}, t)$. We will briefly illustrate the procedure in $d = 2$ where $\mathbf{u} = \begin{pmatrix} \cos\theta \\ \sin\theta \end{pmatrix}$. We expand in Fourier modes $\mathcal{P}(\mathbf{r}, \theta, t)$:

$$\mathcal{P}(\mathbf{r}, \theta, t) = \sum_{n=-\infty}^{+\infty} a_n(\mathbf{r}, t) e^{in\theta} \quad (2.21)$$

such that the zeroth-order mode is the probability we're interested in: $a_0(\mathbf{r}, t) \equiv p(\mathbf{r}, t)$. Projecting then both sides of the Master equation 2.20 onto the n^{th} armonic leads to a dynamical equation for $a_n(\mathbf{r}, t)$ depending on $a_{n\pm1}$, $a_{n\pm2}$: at this point a reasonable approximation is needed to truncate this infinite hierarchy of PDEs. Since the zeroth mode a_0 evolves on diffusive time and length scales ($T \sim L^2$, $R \sim L$), while the higher harmonics $a_{n\neq0}$ exhibit fast exponential relaxation, we assume they quickly reach steady states enslaved to a_0. Additionally, under the assumption of smooth spatial modulations of motility parameters and chemical field, we perform a gradient expansion of the hierarchy. Within the diffusion-drift approximation, we keep only terms up to second-order in spatial derivatives, yielding the scalings $a_{\pm1} \sim \mathcal{O}(\nabla)$, $a_{|n|>2} \sim \mathcal{O}(\nabla^2)$. These assumptions allow us to solve for the lowest harmonics a_0, and ultimately close the hierarchy. A similar procedure can be carried out for active particles in arbitrary dimension d, expanding $\mathcal{P}(\mathbf{r}, \mathbf{u}, t)$ in a base of Harmonic Tensors. We refer to [7] for the detailed computations.

This yields an effective Fokker-Planck equation for $p(\mathbf{r}, t) \equiv a_0(\mathbf{r}, t)$:

$$\partial_t p = -\nabla_{\mathbf{r}} \cdot (\mathbf{V} p - D \nabla_{\mathbf{r}} p) \quad (2.22)$$

with drift velocity and diffusivity given by:

$$\mathbf{V} = -\frac{v_0 \nabla_{\mathbf{r}} v_0}{d(\alpha_0 + (d-1)\Gamma_0)} - \frac{1}{d}\left[v_1 + \frac{v_0(\alpha_1 + (d-1)\Gamma_1)}{\alpha_0 + (d-1)\Gamma_0}\right] \nabla_{\mathbf{r}} c \quad (2.23)$$

$$D = \frac{v_0^2}{d(\alpha_0 + (d-1)\Gamma_0)} + D_t \quad (2.24)$$

The Fokker-Planck equation 2.22 corresponds to the following Langevin dynamics for a single particle's position $\mathbf{r}_i$, valid at space and time scales larger than their persistence length and persistence time respectively:

$$\dot{\mathbf{r}}_i = \mathbf{V}(\mathbf{r}_i) + \nabla_{\mathbf{r}_i} D(\mathbf{r}_i) + \sqrt{2D(\mathbf{r}_i)}\,\boldsymbol{\xi}_i(t) \quad (\text{Itō}) \tag{2.25}$$

where $\boldsymbol{\xi}_i(t)$ is a zero-mean Gaussian white noise with unit variance: $\langle \xi_i(t)\xi_j(t')\rangle = \delta_{ij}\delta(t-t')$. The Itō discretization is made evident since we are dealing with multiplicative noise. Some comments are in order: to start, we note that the drift term $\mathbf{V}$ consists of two contributions. The first one, proportional to $-\nabla_{\mathbf{r}} v_0$, is related solely to quorum sensing and drives particles towards regions where the self-propulsion speed is lower. This is coherent with what found in the previous section, where, in absence of interaction, the probability was found to be inversely proportional to the velocity field. The second term, arising from chemotaxis, biases the motion of the particles towards areas of higher or lower concentration of the chemical, depending on the sign of the prefactor multiplying $\nabla_{\mathbf{r}} c$. Additionally, we remark that, at the mesoscopic level of equation 2.25, whether the particles are ABPs, RTPs, or possess both reorientation mechanisms becomes irrelevant: their respective tumbling and rotational diffusion rates enter the equations only through the combination $\tau_{0(1)}^{-1} \equiv \alpha_{0(1)} + (d-1)\Gamma_{0(1)}$. This equivalence results from truncating the gradient expansion at second order. As a final comment, we point out that deriving the Langevin equation 2.25 from the Fokker–Planck equation 2.22 involves some technical subtleties when the effective diffusivity D is a functional of the density ρ, as in the case of quorum sensing. As shown in [13], this derivation requires adding an extra term to 2.22, proportional to $\nabla K(0)$. This correction vanishes, for instance, when the kernel $K(\mathbf{r})$ is symmetric— a condition that is often satisfied in practice and will be throughout our work.

To complete the coarse graining procedure to a system of N particles one should apply Itō's lemma to obtain a dynamical equation for the local density of particles:

$$\rho(\mathbf{r}, t) = \sum_{i=1}^{N} \delta(\mathbf{r} - \mathbf{r}_i(t)) \tag{2.26}$$

The procedure has been first developed in [5] and results in the fluctuating hydrodynamics for the density $\rho \equiv \rho(\mathbf{r}, t)$:

$$\partial_t \rho = -\nabla_{\mathbf{r}} \cdot \left\{ \mathbf{V}(\mathbf{r}, [\rho])\rho - D(\mathbf{r}, [\rho])\nabla_{\mathbf{r}}\rho + \sqrt{2D(\mathbf{r}, [\rho])\rho}\boldsymbol{\Lambda}(\mathbf{r}, t) \right\} \tag{2.27}$$

which can be recast into the more standard form:

$$\partial_t \rho = \nabla_{\mathbf{r}} \cdot \left[M \nabla_{\mathbf{r}} \mathfrak{u} + \sqrt{2M}\boldsymbol{\Lambda} \right] \tag{2.28}$$

with effective mobility and out-of-equilibrium chemical potential:

$$M \equiv M(\mathbf{r}, [\rho]) = D(\mathbf{r}, [\rho])\rho(\mathbf{r}) \tag{2.29}$$

$$\mathfrak{u} \equiv \mathfrak{u}(\mathbf{r}, [\rho]) = \log \rho(\mathbf{r}) + \frac{1}{2}\log D(\mathbf{r}, [\rho]) + \left(v_1 + v_0(\mathbf{r}, [\rho])\frac{\tau_0}{\tau_1} \right) \frac{c(\mathbf{r}, [\rho])}{dD} \tag{2.30}$$

We stress that the macroscopic description of equation 2.28 was derived within the assumption of slowly varying spatial modulation of motility, and is therefore valid only at large length scales—specifically, at scales larger than the persistence length l_p of the particles. The diffusion-drift approximation breaks down when self-organization instead occurs at or below the scale given by l_p.

2.6 Free Energy and mapping to equilibrium system

The field dynamics 2.28 is an equilibrium one if it admits a free energy $\mathcal{F}$ such that $\mathfrak{u} = \frac{\delta \mathcal{F}}{\delta \rho}$, *i.e.* if the Schwartz theorem generalized to functionals holds:

$$\frac{\delta \mathfrak{u}(\mathbf{r}', [\rho])}{\delta \rho(\mathbf{r})} - \frac{\delta \mathfrak{u}(\mathbf{r}, [\rho])}{\delta \rho(\mathbf{r}')} = 0 \tag{2.31}$$

For the moment, we will carry out the calculation of $\mathcal{F}$ in the case of chemotaxis only, where v_0, α_0, $\Gamma_0 \in \mathbf{R}$, and with c a linear functional of the density, as given by equation 2.13. We get:

$$\mathfrak{u}(\mathbf{r}, [\rho]) = \log \rho(\mathbf{r}) + \left(v_1 + v_0 \frac{\tau_0}{\tau_1} \right) \frac{c(\mathbf{r}, [\rho])}{dD} \tag{2.32}$$

Schwartz theorem is satisfied whenever $\frac{\delta c(\mathbf{r}', [\rho])}{\delta \rho(\mathbf{r})} = K(\mathbf{r}' - \mathbf{r}) = K(\mathbf{r} - \mathbf{r}') = \frac{\delta c(\mathbf{r}, [\rho])}{\delta \rho(\mathbf{r}')}$, that is, when we are dealing with a symmetric kernel. If so, we can functionally integrate equation 2.32 and obtain:

$$\mathcal{F}[\rho] = \int \rho(\mathbf{r})(\log \rho(\mathbf{r}) - 1)\, d\mathbf{r} + \left(v_1 + v_0 \frac{\tau_0}{\tau_1} \right) \frac{1}{2dD} \int d\mathbf{r} d\mathbf{r}' \rho(\mathbf{r}) K(\mathbf{r} - \mathbf{r}') \rho(\mathbf{r}') \tag{2.33}$$

Remarkably, starting from a passive system of N colloidal particles, each obeying a Langevin equation[1]:

$$\gamma \dot{\mathbf{r}}_i = -\sum_{j \neq i} \nabla_{\mathbf{r}_i} V(\mathbf{r}_i - \mathbf{r}_j) + \sqrt{2T} \boldsymbol{\eta}_i(t) \tag{2.34}$$

where $\boldsymbol{\eta}_i(t)$ is a unitary white Gaussian noise, one could coarse grain the dynamics to obtain the same fluctuating hydrodynamics equation 2.28, provided that:

$$\frac{T}{\gamma} = D \qquad \frac{V(\mathbf{r} - \mathbf{r}')}{\gamma} = \frac{1}{d} \left(v_1 + v_0 \frac{\tau_0}{\tau_1} \right) K(\mathbf{r} - \mathbf{r}') \tag{2.35}$$

This mapping has been established in [11] and expresses the fact that, although the microscopic dynamics of tactic active particles and passive colloids are fundamentally different, their large-scale behaviour is completely equivalent, and all the macroscopic phenomenology arising in passive systems can be observed in tactic active ones as well.

[1] Note that here and in all the following Temperature is expressed in units of Boltzmann constant k_B.

2.7 Predict MIPS from free energy

After having derived the free energy for chemotactic systems in the previous paragraph, we now show that the same computation for quorum sensing interactions (with $v_1 = \alpha_1 = \Gamma_1 = 0$) is not always possible. For simplicity we take $D_t = 0$. Up to constant terms, the chemical potential simplifies to:

$$\mathfrak{u}(\mathbf{r}, [\rho]) = \log \rho(\mathbf{r}) + \log v_0(\mathbf{r}, [\rho]) \tag{2.36}$$

which is clearly non-local, due to the functional dependence of v_0 on the full density field. This non-locality generally prevents the existence of a free energy $\mathcal{F}$ for arbitrary $v_0(\rho)$. Nevertheless, assuming that the typical length scale of the coarse-graining kernel K—*i.e.* the distance over which the chemical produced by an active particle is sensed by the others—to be much smaller than the scale over which ρ varies, we can expand:

$$\begin{aligned} c(\mathbf{r}, [\rho]) &= \int d\mathbf{r}' K(\mathbf{r} - \mathbf{r}')\rho(\mathbf{r}') && (2.37)\\ &\approx \int d\mathbf{r}' K(\mathbf{r} - \mathbf{r}') \left(\rho(\mathbf{r}) + (\mathbf{r}' - \mathbf{r})\nabla_{\mathbf{r}}\rho(\mathbf{r}) + \frac{1}{2}(\mathbf{r}' - \mathbf{r})\mathbf{H}(\mathbf{r})(\mathbf{r}' - \mathbf{r}) \right) && (2.38)\\ &= \hat{K}(0)\rho(\mathbf{r}) + \mathcal{O}(\nabla^2\rho) && (2.39) \end{aligned}$$

where $\mathbf{H}$ is the Hessian of ρ, we have defined $\hat{K}(0) = \int d\mathbf{r} K(\mathbf{r})$ and we have used the fact that K is symmetric. The local approximation consists in truncating the expansion at zeroth order, such that the self-propulsion speed at a given point depends only on the local density in that point. It corresponds to take the Kernel to be a delta function, weigthed by its norm (the area under its curve). The large-scale dynamics then reduces to an equilibrium one with free energy and free energy density:

$$\mathcal{F}[\rho] = \int d\mathbf{r} f(\rho(\mathbf{r})) \qquad \text{with} \qquad f(\rho) = \rho(\log \rho - 1) + \int^{\rho} d\tilde{\rho} \log v_0(\tilde{\rho}) \tag{2.40}$$

As in equilibrium physics, the most likely state minimizes $\mathcal{F}$. In the following we revise the computations in [12] that show how minimization of free energy can explain the instability of a uniform density profile, leading to the separation of the system into two phases with densities $\rho_l > \rho_g$.
Indeed, a phase-separated system with a gas fraction α and a liquid fraction $1 - \alpha$ would have $\mathcal{F} = \mathcal{V}\left(\alpha f(\rho_l) + (1 - \alpha) f(\rho_g)\right)$ where $\mathcal{V}$ is the total volume. We will therefore require minimization of the constrained free energy density:

$$G(\rho_l, \rho_g, \alpha, \mu) = \alpha f(\rho_g) + (1 - \alpha) f(\rho_l) - \mu\left(\rho_0 - \alpha\rho_g - (1 - \alpha)\rho_l\right) \tag{2.41}$$

where the Lagrange multiplier μ enforces conservation of mass. Taking derivatives we obtain:

$$\frac{\partial G}{\partial \rho_l} = \frac{\partial G}{\partial \rho_g} = 0 \quad \Leftrightarrow \quad f'(\rho_g) = f'(\rho_l) = \mu \tag{2.42}$$

$$\frac{\partial G}{\partial \alpha} = 0 \quad \Leftrightarrow \quad f(\rho_g) - \mu\rho_g = f(\rho_l) - \mu\rho_l \tag{2.43}$$

$$\frac{\partial G}{\partial \mu} = 0 \quad \Leftrightarrow \quad \alpha = \frac{\rho_l - \rho_0}{\rho_l - \rho_g} \tag{2.44}$$

The first two equations are satisfied if f admits a common tangent construction, that is if there exist two points $(\rho_g, f(\rho_g))$ and $(\rho_l, f(\rho_l))$ sharing the same tangent, which requires f to be non-convex. Being $\alpha \in [0, 1]$, the third equation shows that coexistence occurs when $\rho_0 \in [\rho_g, \rho_l]$, defining the binodal region pictured in Figure 2.2c. Within this interval, we identify the spinodal region $\left[\rho_g^s, \rho_l^s\right]$, where $\frac{\partial^2 f}{\partial \rho^2} < 0$. In this window, a uniform profile is unstable because small fluctuations bring a uniform systems at ρ_0 to separate into two regions at slightly perturbed densities $(\rho_0 + \delta\rho_1)$, $(\rho_0 - \delta\rho_2)$, lowering the global free energy and triggering spinodal decomposition, as shown in Figure 2.2d. Outside this interval but still within the binodals, *i.e.* for $\rho_0 \in \left[\rho_g, \rho_g^s\right] \cup [\rho_l^s, \rho_l]$, the uniform profile is metastable and nucleation is required to initiate phase-separation. For the quorum sensing field theory 2.40 the condition for spinoidal instability is:

$$\frac{\partial^2 f}{\partial \rho^2} = \frac{1}{\rho} + \frac{v_0'(\rho)}{v_0(\rho)} < 0 \tag{2.45}$$

which is the same that we have previously derived with heuristic arguments in section 2.4.

We have tried to apply the framework of common tangent construction to chemotactic interactions as well. In this case, one can carry out a local approximation to equation 2.33, obtaining a free energy and free energy density:

$$\mathcal{F}[\rho] = \int d\mathbf{r} f(\rho(\mathbf{r})) \qquad \text{with} \qquad f(\rho) = \rho(\log\rho - 1) + \frac{1}{2}\underbrace{\frac{1}{dD}\left(v_1 + v_0\frac{\tau_0}{\tau_1}\right)}_{k}\hat{K}(0)\rho^2 \tag{2.46}$$

Such free energy density is non convex only when $k\hat{K}(0) < 0$, as it is depicted in Figure 2.2f. Although, even in the non convex case, it does not admit a common tangent construction, since the energy term scales out the entropic term: $\rho\log\rho \ll \rho^2$ as $\rho \gg 1$. Therefore, the local approximation fails completely in describing phase separation when starting from a high enough average density, only predicting a condensation of the liquid phase at unbounded ρ_l, while $\rho_g \to 0$. This behavior will indeed be observed in simulations presented in section 3.2. More precisely, the local approximation ignores the existence of a structure in the dense phase. When correctly resolved, the latter can lead to the stabilization of a liquid-gas coexistence, with finite densities for both gas and liquid phases.

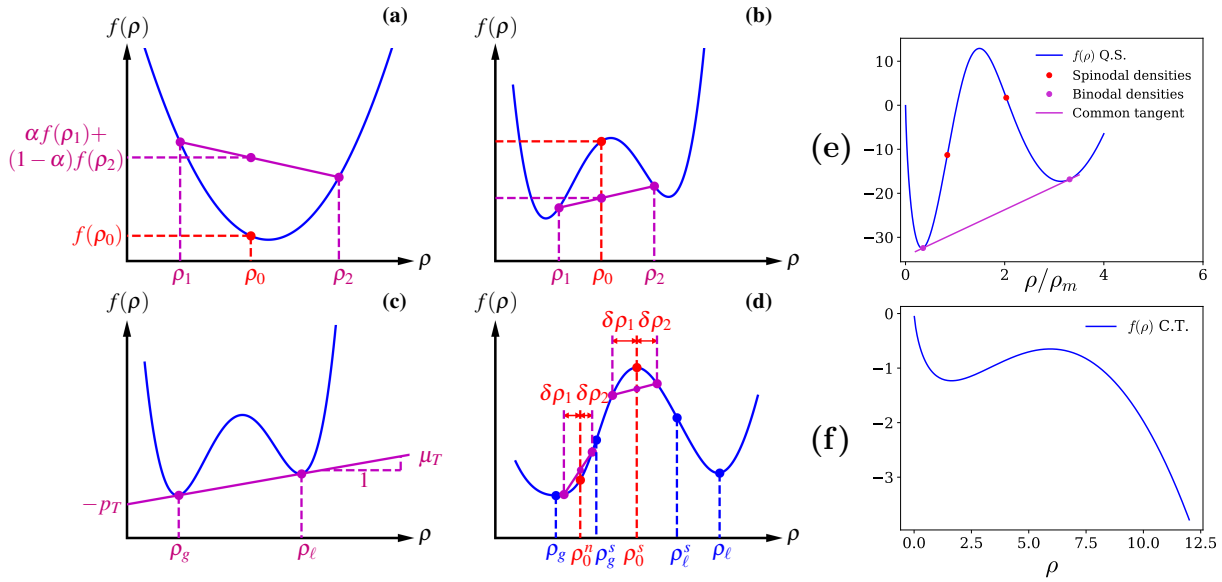

Figure 2.2: (**a**)-(**d**) Prediction of phase separation with common tangent construction, image from [12]: (**a**) If the free energy density $f(\rho)$ is everywhere convex, any uniform density ρ_0 is stable, since any separation in densities ρ_1, ρ_2 such that $\rho_0 = \alpha\rho_g + (1-\alpha)\rho_l$ would increase the total free energy of the system. (**b**) When f is concave around the initial density ρ_0 the uniform profile is unstable because separation into densities ρ_1, ρ_2 can lower the total free energy. (**c**) Common tangent construction identifies the binodal densities ρ_g, ρ_l. (**d**) The condition $\frac{\partial^2 f}{\partial \rho^2} < 0$ marks the spinodal region. If initial density ρ_0 lies inside this interval a weak perturbation leading to densities $\rho_0 + \delta\rho_1$, $\rho_0 - \delta\rho_2$ is sufficient to destabilize the uniform profile, being energetically favored. On the contrary, when $\rho_0 \in [\rho_g, \rho_g^s] \cup [\rho_l^s, \rho_l]$ nucleation is required. (**e**) Effective free energy density within the local approximation for the quorum sensing system, obtained by inserting the self propulsion speed 3.3 with $v_g = 10$, $v_l = 1$ into the function 2.40. Common tangent construction is successful in predicting phase separation and giving an estimate for the binodal densities. (**f**) Local approximation of free energy density for chemotactic system with $k = -0.3$: no common tangent can be constructed.

Chapter 3

Numerical simulations of monodisperse system

We have developed a code to perform numerical simulations of the system at the microscopic particle level. At first, we simulated a 1-dimensional system, in which N RTPs live in a box of size L with periodic boundary conditions. For every particle, a time duration of the next run phase is randomly drawn from an exponential distribution of mean τ, then, when a tumbling event occur during a timestep dt, the particle position is updated for the corresponding fraction of dt, its direction is inverted with probability $1/2$, and position is then again updated until the end of the timestep. Interactions among particles are mediated by the chemical field which, in practice, can be computed as follows:

$$c(x) = (K*\rho)(x) = \int_0^L dx' K(x-x')\rho(x') = \int_0^L dx' K(x-x') \sum_{i=1}^{N} \delta(x_i - x') = \sum_{i=1}^{N} K(x-x_i) \tag{3.1}$$

The sole self-propulsion speed undergoes regulation according to equation 2.7, while the tumbling rate τ^{-1} is kept constant (in the notation adopted in this report, $\alpha_1 = 0$). We set $D_t = 0$, meaning that particles do not diffuse, which is a sensible assumption for bacteria, as we showed in section 2.1. We chose a coarse-graining kernel K with typical length scale σ, representing the interaction length. Consequently, the timestep dt of the simulation is computed adaptively at every step such that the maximal displacement never exceeds $\sigma/10$. This method ensures that the timestep is low enough to properly resolve interactions. The code is kept $\mathcal{O}(N)$ by tracking the positions of particles inside virtual boxes of the size of the interaction length, such that interactions only occur among particles in the same box or in nearest neighboring boxes. Results are shown in terms of a smoothed density of particles $\hat{\rho}$, possibly averaged over a number of decorrelated samples:

$$\rho(x) = \sum_{i=1}^{N} \delta(x - x_i) \quad \approx \quad \hat{\rho}(x) = (g*\rho)(x) = \int dx' g(x-x')\rho(x') = \sum_{i=1}^{N} g(x-x_i) \tag{3.2}$$

where g is a smoothing kernel.

3.1 Quorum sensing

To begin with, the code has been tested on the well studied situation of quorum sensing. To compare with results in [12, 14], the same motility regulation has been employed:

$$v(x,[\rho]) = v_g + \frac{v_l - v_g}{2}\left[1 + \tanh\left(2\frac{c(x,[\rho]}{\rho_m} - 2\right)\right] \tag{3.3}$$

where $v_g > v_l$, $\rho_m \in \mathbf{R}^{\geq 0}$ are parameters to be chosen. The speeds v_g and v_l are the limiting velocities of the particles when the local density is, respectively, $\rho \ll \rho_m$ or $\rho \gg \rho_m$. Such regulation slows down active particles in response to crowding, fueling the positive feedback that leads to MIPS. The chemical concentration c is obtained by convoluting the empirical density with the bell-shaped kernel:

$$K(x) = \frac{A}{\sigma} e^{-\frac{\sigma^2}{\sigma^2 - x^2}} \Theta(\sigma^2 - x^2) \tag{3.4}$$

where A is a normalizing constant and Θ is the Heaviside step function. Such function resembles qualitatively a Gaussian but has the advantage that its derivative of all order (including the function itself) vanish for $x = \pm\sigma$, making it particularly suitable for a numerical simulation where a threshold interaction length must be set to limit the computational complexity. The system is initialized at a uniform average density ρ_0 so that, when the latter is chosen in the to-be-found binodal interval $\rho_0 \in [\rho_g, \rho_l]$, the system separates into coexisting gas and liquid phases, as illustrated by the snapshots in Figure 3.1b. We measured their densities ρ_g and ρ_l via identifying the position of the peaks in the histograms of density values collected in every point of the box and over many decorrelated time samples. We summarize in Figure 3.1 our results of the binodal densities (green triangles) for various values of the ratio v_g/v_l, alongside theoretical predictions and previously published data from [14].

Our numerical results closely match those from earlier simulations and exhibit even better agreement with the theoretical predictions developed in [12].

3.2 Chemotaxis

In this section we will present the main simulation results of this report, focusing on chemotaxis. We simulated chemotactic interactions among the Run-and-Tumble particles by regulating their speed according to:

$$v = v_0 - v_1 u \, \partial_x c(x,[\rho]) \tag{3.5}$$

where $v_0,\ v_1 \in \mathbb{R}$ are tunable parameters and $u \in [-1, 1]$. As before, the tumbling rate is constant $\tau = \tau_0$. Following the same logic of equation 3.1:

$$\partial_x c(x) = \sum_{i=1}^{N} K'(x - x_i) \tag{3.6}$$

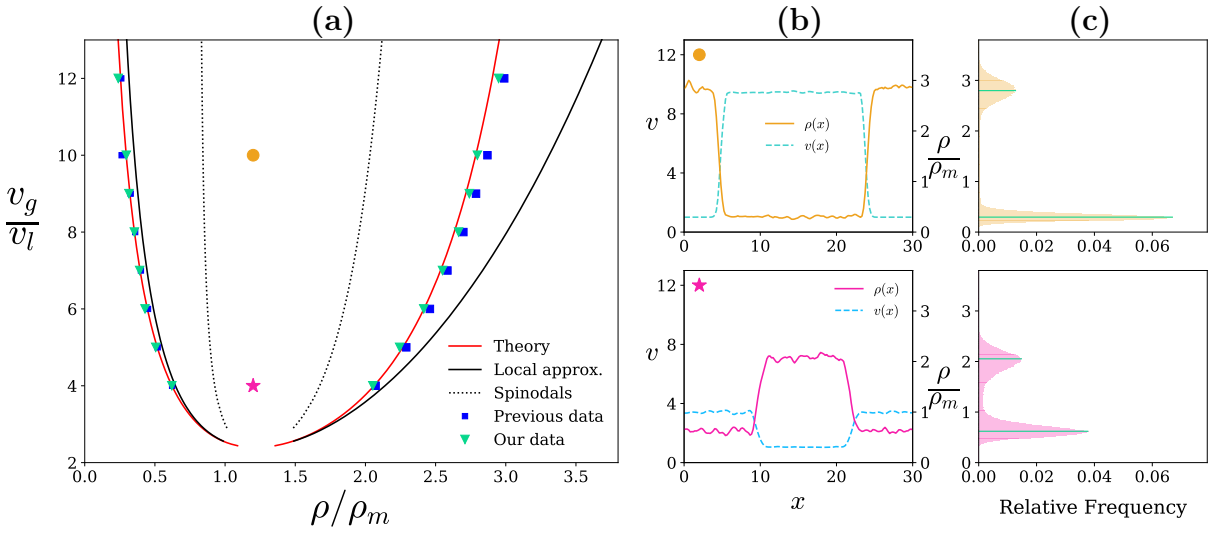

Figure 3.1: Simulations with quorum sensing regulation of self-propulsion speed. (**a**) Phase diagram of the system in the plane $(\rho/\rho_m,\ v_g/v_l)$. The solid and dotted black lines represent the binodals and spinodals, respectively, computed using the common tangent construction within the local approximation (see Sec. 2.7). The red curve corresponds to a mean-field theory developed in Ref. [14], from which the blue square data points are also adapted. Green triangles are our numerical results. (**b**) and (**c**) Examples of simulations at $v_g/v_l = 10$ (top) and $v_g/v_l = 4$ (bottom). (**b**) Spatial profiles of density $\rho(x)$ and speed $v(x)$, obtained by averaging 10 snapshots spaced out by a decorrelation time of 10τ, used solely for presentation purposes to slightly smooth out fluctuations. (**c**) Histograms of local density values collected over 1000 decorrelated snapshots. Peaks at maximal values of the histogram correspond to the coexisting densities plotted in panel (a). Parameters common to all simulations: $L = 30,\ \sigma = 1,\ \tau = 1,\ v_l = 1,\ \rho_m = 100,\ \rho_0 = 120$.

We remind that the chemotactic active system is equivalent, at the macroscopic scale, to a system of passive colloids with friction coefficient γ at temperature T, interacting through a potential V. Applying our choice of parameters and dimensionality, the correspondence detailed in equation 2.35 is established provided that:

$$V(x) = \gamma v_1 K(x) \qquad T = \gamma D = \gamma v_0^2 \tau_0 \tag{3.7}$$

3.2.1 Condensation

We studied the system given by the bell-shaped coarse graining kernel 3.4, represented in Figure 3.2a. The corresponding equilibrium system interacts via a potential that is either a well, if $v_1 < 0$, or a hill, if $v_1 > 0$. Accordingly, we expect the active system to collapse into points in the first case, or to remain in a uniform phase where particles maximize their mutual distances in the second. Indeed, these behaviors are observed in numerical simulations, as shown in Figure 3.2b, and agree with the prediction given by a local approximation of the free energy. Collapse can occur via two distinct mechanisms. Applying the instability criterion derived in Section 4.3 to the bell-shaped kernel (for which $\hat{K}(q) > 0 \ \forall q$), one finds that the system is predicted to become unstable to fluctuations when:

$$k = \frac{v_1}{v_0^2 \tau_0} < -\frac{1}{\rho_0 \hat{K}(0)} \tag{3.8}$$

In this regime, spinodal decomposition is expected: multiple droplets of condensed matter spontaneously form independently and subsequently merge over time. In contrast, when $-\frac{1}{\rho_0 \hat{K}(0)} < k < 0$ the system is stable with respect to small fluctuations. However, the uniform density phase is only meta-stable, and condensation can still occur through nucleation: a single droplet spontaneously forms and, being "energetically" favored, gradually absorbs all other particles. The difference between these two regimes is illustrated in Figure 3.2b.

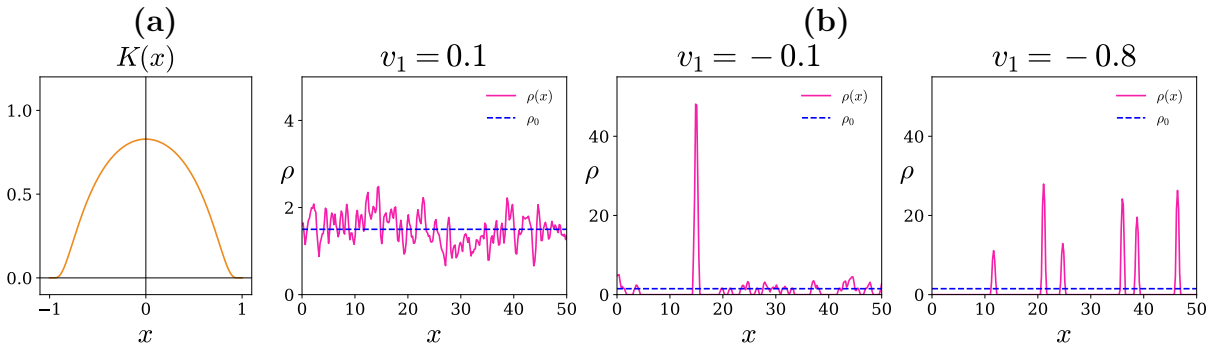

Figure 3.2: Simulations with chemotactic interactions with bell-shaped kernel. (**a**) Coarse-graining kernel. (**b**) Time average of 20 snapshots of density profile (in pink) in the regime $k > 0$ (left), instantaneous snapshots in the regimes $-\frac{1}{\rho_0} < k < 0$ (center), $k < -\frac{1}{\rho_0}$ (right) and average density (dashed blue line). Homogeneous phase at equilibrium, nucleation and spinodal decomposition at early stages ($t = 100\tau$), respectively, are observed. Parameters common to the three simulations: $L = 50,\ \sigma = 1,\ \tau = \tau_0 = 1,\ v_0 = 1,\ \rho_0 = 1.5$.

3.2.2 Phase coexistence

We next investigated the interacting system given by a composite kernel:

$$K(x) = \frac{1}{2l_r} e^{-\frac{|x|}{l_r}} - \frac{\varepsilon}{2l_a} e^{-\frac{|x|}{l_a}} \tag{3.9}$$

where $l_r > l_a$, setting the interaction length to $\sigma = l_r$. Such a kernel cannot derive from the dynamics of one chemical fields, since, depending on the value of ε, can assume negative values which could lead to unphysical negative values for the concentration c. In order to understand the reason for this choice, we consider a modulating mechanism based on two chemicals in the environment:

$$\begin{aligned} v &= v_0 - v_{11} u\, \partial_x c_1(x) - v_{12} u\, \partial_x c_2(x) \\ &= v_0 - v_{11} u\, \partial_x (K_1 * \rho)(x) - v_{12} u\, \partial_x (K_2 * \rho)(x) \\ &= v_0 - v_{11} u\, \partial_x (K * \rho)(x) \qquad \text{where} \qquad K(x) = K_1(x) + \frac{v_{12}}{v_{11}} K_2(x) \end{aligned}$$

It is clear then that the kernel 3.9 represented in Figure 3.3e mimics the situation in which two chemical fields with the exponential kernel of equation 2.11 are present: choosing $v_1, \varepsilon > 0$ describes RTPs repelled by the chemical with length scale l_r ($v_{11} > 0$) and attracted by the one with length scale l_a ($v_{12} < 0$).

In the language of the equivalent passive system, we are studying interactions composed of hard-core repulsion and attractive tails, similar to the ones in a Van der Waals fluid. We expect then to find the phase diagram in space (ρ, T) of Figure 3.3a, where lowering the temperature below a critical line triggers phase separation. For densities comprised between the spinodal and binodal lines a uniform density profile is still metastable, even though not energetically favored. In contrast with what is typically done, the effective temperature of the active system was set constant in the simulations by fixing v_0 and τ_0, while ε has been varied to control the depth of the attractive tails. Increasing ε produces deeper wells and so, to some extent, the same effect of lowering the temperature as $1/\varepsilon$, leading to phase separation of the system into coexisting gas and liquid phases, shown by the snapshots in Figure 3.3c. Indeed, the system transitions from a constant density state (blue) to a separated state (orange). When ε is increased enough so that $\hat{K}(0) = \int dx K(x) < 0$, *i.e.* $\varepsilon > 1$, according to the local approximation of free energy, the system is predicted to collapse, with particles condensating to arbitrary high density, as visible in the pink snapshot.

In order to measure the coexisting densities ρ_g, ρ_l, given the intrinsically discrete nature of numerics simulating particles (and not the continuous field ρ), one would need a bin size $l \gg 1/\rho_g,\ 1/\rho_l$, such that a high enough number of particles fall inside the bin (or equivalently the typical lengthscale of the plotting kernel g). However, a proper phase transition in the statistical mechanical sense, cannot be achieved in $1d$, due to the relative scalings between energy and entropy of the ordered state, exactly as happens for the Ising model in one dimension. Therefore, a one-domain configuration with long-range correlations is non-favored, instead, the system separates into droplets with typical size l_d, making it necessary to reduce the binning size l in the plots 3.3c in order to resolve them. This sets a minimal threshold density, drawn in green in panel 3.3d, below which densities cannot be resolved and measured. In particular, in our system, l_d and ρ_g are such that an optimal binning length l such that $1/\rho_g \ll l \ll l_d$ does not exist, making

it impossible to measure ρ_g. For this reason we have implemented 2d simulations of the system, which results are accounted in section 3.3.

As a final remark, we note that, given our choice of $k > 0$, the mean field theory developed in section 4.3 predicts the onset of a linear instability of the uniform density profile when:

$$\exists q \text{ s.t. } \hat{K}(q) < -\frac{1}{k\rho_0} \tag{3.10}$$

where $\hat{K}(q)$ is the Fourier transform of the kernel $K(x)$ and $k = \frac{v_1}{v_0^2 \tau_0}$ is positive. This condition is marked by the dashed black line in Figure 3.3b, below which the uniform profile is unstable. In particular, the condition requires $\varepsilon > 1$, for which the system undergoes thermodynamic collapse, and thus is not able to distinguish the phase separated region.

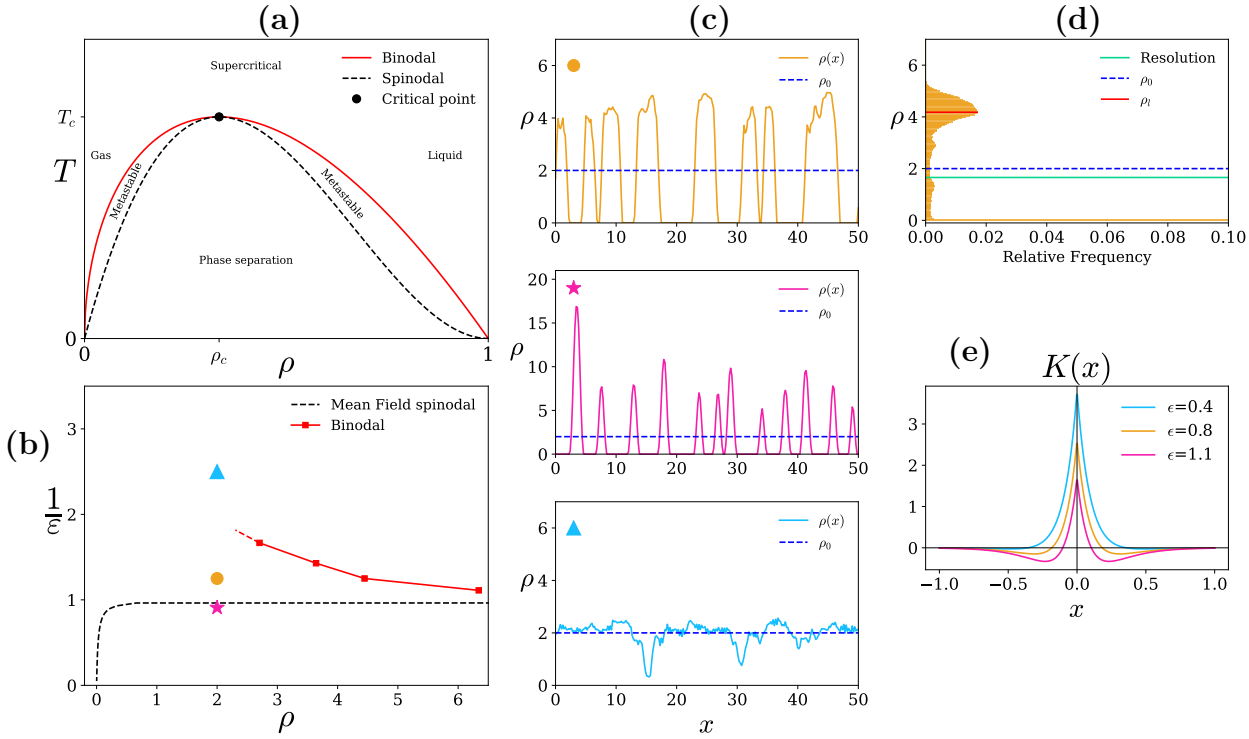

Figure 3.3: (**a**) Qualitative sketch of the phase diagram in the space (ρ, T) of the passive system. (**b**) Phase space of the chemotactic system in the corresponding variables $(\rho, 1/\varepsilon)$, where the dashed black line is the spinodal density obtained from linear stability analysis in Mean Field. (**c**) Spatial density profile with $\rho_0 = 2$ (dashed blue line) in different regimes: in blue (bottom) time average of 30 decorrelated snapshots at $\varepsilon = 0.4$ corresponding to a constant density phase, in orange (top) instantaneous snapshot at $\varepsilon = 0.8$, where phase separation occur, in pink (center) instantaneous shot at $\varepsilon = 1.1$ showing thermodynamic collapse. (**d**) Histogram of values of local densities from 700 decorrelated snapshots. The green line marks the minimal density that can be resolved due to the smoothing process necessary to plot profiles in one dimension. The red line identies the peak density, corresponding to the binodal density ρ_l marked in red in panel (b).(**e**) Coarse-graining kernel for the 3 values of ε considered in panel (b) and (c). Parameters common to all simulations: $L = 50,\ v_0 = 0.5,\ v_1 = 1,\ \sigma = 1,\ \tau = 0.1,\ l_r = 1/10,\ l_a = 1/6$ leading to $k = 40$.

3.3 2d simulations

Since 1d simulations of the chemotactic system have proven to be problematic due to the lack of a proper phase transition, combined with an extremely low density of the gas phase, we have extended the code to simulate the same system in two spatial dimensions. The N RTPs live in a square box of side L with periodic boundary conditions. Their orientation vector $\mathbf{u}$ is determined by an angle θ and, at each tumble, a new direction θ' is drawn uniformly in $[0, 2\pi]$. At every timestep the sole self propulsion speed is regulated via computing the gradient of the chemical field in each particles' position. Since the Kernel is always taken to be rotationally invariant, interactions depend only on the distance d between particles:

$$\nabla_{\mathbf{r}} c(\mathbf{r}) = \sum_{i=1}^{N} \nabla_{\mathbf{r}} K(\mathbf{r} - \mathbf{r}_i) = \sum_{i=1}^{N} \frac{\partial K}{\partial d_i} \frac{\mathbf{r} - \mathbf{r}_i}{d_i} \tag{3.11}$$

in the exact same way in which one would compute pairwise forces with a potential proportional to K, coherently with the equilibrium mapping. We have again chosen positive v_1 and a composite kernel representing the interplay between an attractive and a repulsive chemical field with lengthscales, respectively, l_a and l_r:

$$K(d) = a_r K_0\left(\frac{d}{l_r}\right) - a_a K_0\left(\frac{d}{l_a}\right) \tag{3.12}$$

where we remind that K_0 is the 0^{th} order modified Bessel function of the second kind. We have fixed the parameters $a_{a(r)}$, $l_{a(r)}$ so that the system is equivalent, at large scales, to an equilibrium system of passive particles interacting through a potential with soft core repulsion and slightly attractive tails. Additionally, $\hat{K}(\mathbf{q}) > 0\ \forall \mathbf{q}$, so that the dynamical instability condition derived in section 4.3 translates to:

$$k < -\frac{1}{\rho_0 \min_{\mathbf{q}} \hat{K}(\mathbf{q})} \tag{3.13}$$

and is never satisfied, being $k \propto v_1 > 0$. Of course, this does not guarantee in any way that the system will remain in a uniform phase for two main reasons: first, the linear stability analysis gives a dynamical criterion which does not capture the possibility of metastability, that occurs when the uniform state is a local minimum of the constrained free energy but not a global one. Additionally, the criterion comes from a mean field approximation, which is, by definition, uncontrolled.

Indeed, simulations show phase separation of the system into coexisting gas and liquid phases, with droplets of liquid slowly merging into a single domain over time. To produce a phase diagram that is the closest possible to the equilibrium system's one, we have kept the coarse graining kernel fixed and changed the persistence time τ of active particles, which is directly proportional to the effective Temperature. Increasing τ then, one expects to cross a critical line, above which the uniform profile is stable. As visible from the snapshots in Figure 3.4, the gas density can so low that identifying a binning length l much larger than $1/\rho_l$ and $1/\rho_g$ but much smaller than the droplet size seems complicated. Therefore, in order to measure the binodal densities $\rho_l(\tau)$, $\rho_g(\tau)$ we have employed a different strategy.

Taking a time snapshot of the system, we have run a clustering algorithm on the data constituted by 2-dimensional positions of particles at that time. The algorithm should not only be able to identify clusters of similar density, irrespectively of their shape, but also to leave out particles that do not belong to any cluster, which will be identified as particles in the gas phase. Therefore, the natural choice was to use the DBSCAN clustering algorithm, first introduced in [8], that builds on the two hyperparameters ϵ and minPts: a points is defined as a core point if at least minPts are present in its spherical neighborhood of radius ϵ. Then a point belong to a cluster either if it is a core points or if it is in the ϵ-neighborhood of a core point. ϵ and minPts have been chosen to achieve stability of the classification.

At the end of the clustering procedure one can distinguish particles belonging to liquid and gas phases, the next step is then measuring the area of the liquid droplets. Since the latter can be highly non convex, especially at high effective temperatures, we have computed the alpha-shape of every cluster, which is a generalization of the concept of the convex-hull and leads to a non convex polygon for every cluster, which area and consequent density can be readily evaluated. At the end of the procedure one will obtain one sample of ρ_l for each cluster and one sample of ρ_g computed by dividing the number of non-clustered points by the area left out by clusters. Finally the binodal densities can be extracted as averages of the values collected over many time samples, constructing (partially) the phase diagram in space (τ, ρ). Two example pictures of the method are reported in Figure 3.4 for different effective temperatures, along with one corresponding histogram and the phase diagram in Figure 3.5.

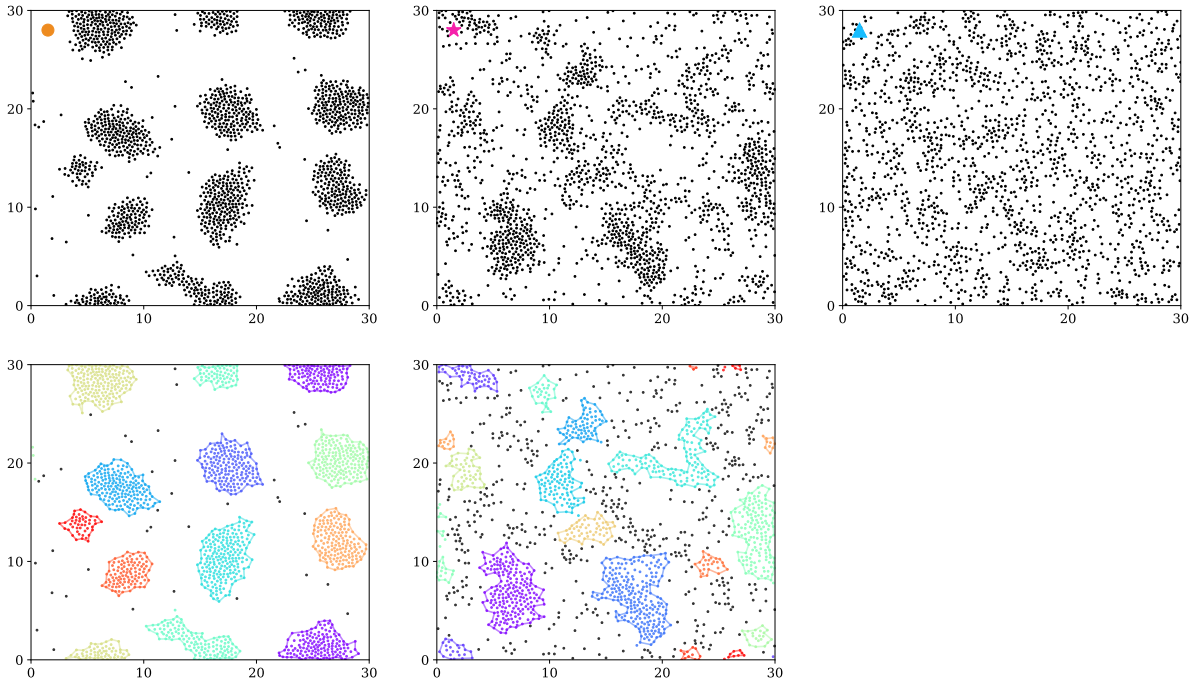

Figure 3.4: Instantaneous snapshots of the system of RTPs at different values of τ (and therefore effective temperature): $\tau = 0.02$ (left), $\tau = 0.04$ (center), $\tau = 0.06$ (right). The bottom panel illustrates with different colors the clusters identified by DBSCAN (note that PBCs have been applied for the color coding), contoured by the corresponding AlphaShape. Black points are particles in the gas phase. Colored shapes in the top panel reference to phase diagram of Figure 3.5. Parameters common to all simulations: $v_0 = 1$, $v_1 = 1.3$, $a_r = 2$, $a_a = 0.5$, $l_r = 1/7.5$, $l_a = 1/4$, $\sigma = 1$, $\rho_0 = 2$, $L = 30$.

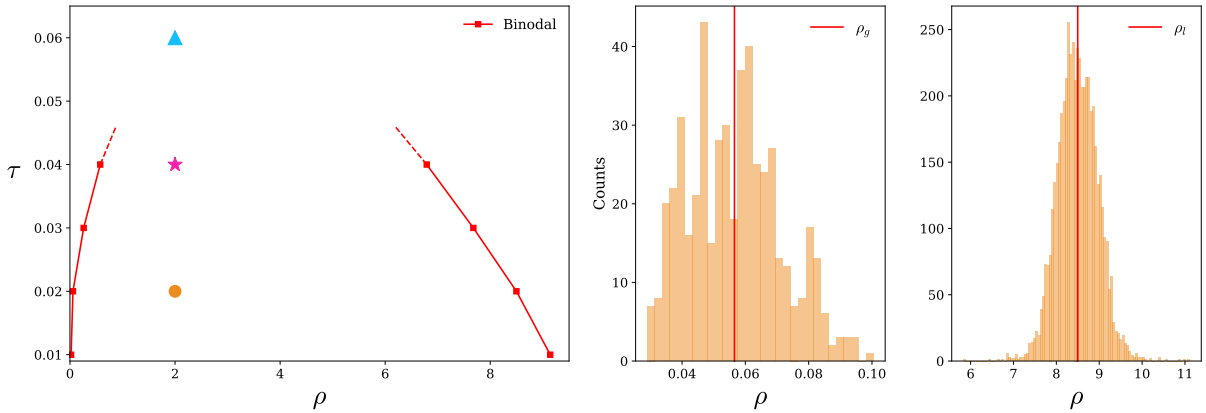

Figure 3.5: Phase diagram (left) of the chemotactic system in space (τ, ρ) corresponding to the equilibrium system in space (T, ρ). Red points are the liquid and gas binodal densities measured as averages of the histograms (right) of values collected over many time samples. The histograms (right) exemplifies the analysis carried out for the system at $\tau = 0.02$. The colored points mark the parameter choice for the three simulations shown in figure 3.4.

Chapter 4

Active mixtures

In the following we turn our attention to active mixtures, namely systems composed of multiple strains of particles, each characterized by distinct motility parameters. Our focus is on high-dimensional ecosystems, meaning those with a large number S of strains, which are particularly relevant in theoretical ecology. In many biological systems of this kind, notably microbial communities, motility is regulated through specific signalling pathways that couple different strains. In addition to these systematic interactions, motility can also be affected by weaker, indirect mechanisms, such as the exchange of metabolites between strains. Since biological systems are inherently complex, modeling these mild effects in full detail would not only be impractical but also of limited theoretical interest: our goal is to understand the typical behavior of such ecosystems. For this reason, we model these indirect interactions as random couplings, treating them as quenched disorder, and investigate how the system behaves independently of the specific realization of the disorder.

4.1 Generalization of coarse graining

In this paragraph we will briefly generalize the coarse-graining methods outlined in section 2.5 to mixtures of S strains. We allow for both quorum sensing and chemotaxis, based on multiple chemical fields $c_h(\mathbf{r}, [\{\rho_\mu\}])$ with $h \in \{1, \dots, H\}$. Self-propulsion speed and persistence time of particle i of strain μ located at $r_{i\mu}$ are then a function of the fields in the same position:

$$v_{i\mu} = v_{0\mu}(\{c_h\}) - \mathbf{u}_{i\mu} \cdot \sum_{h=1}^{H} v_{1\mu}^h \nabla_{\mathbf{r}_{i\mu}} c_h \tag{4.1}$$

$$\tau_{i\mu}^{-1} = \tau_{0\mu}^{-1}(\{c_h\}) + \mathbf{u}_{i\mu} \cdot \sum_{h=1}^{H} (\tau_{1\mu}^h)^{-1} \nabla_{\mathbf{r}_{i\mu}} c_h \tag{4.2}$$

We do not distinguish between different reorienting mechanisms (RTPs or ABPs) since their equivalence at the fluctuating hydrodynamic level will remain valid. With analogous calculations the Langevin equation for the density of strain μ is obtained:

$$\partial_t \rho_\mu = -\nabla_{\mathbf{r}} \cdot \left\{ \mathbf{V}_\mu(\mathbf{r}, \{\rho_\nu\})\rho_\mu - D_\mu(\mathbf{r}, \{\rho_\nu\}) \nabla_{\mathbf{r}} \rho_\mu + \sqrt{2D_\mu(\mathbf{r}, \{\rho_\nu\})\rho_\mu} \mathbf{\Lambda}_\mu(\mathbf{r}, t) \right\} \tag{4.3}$$

$$\mathbf{V}_\mu = -\frac{v_{0\mu}\nabla_{\mathbf{r}} v_{0\mu}}{d(\tau_{0\mu})^{-1}} - \frac{1}{d}\sum_{h=1}^{H}\left[v_{1\mu}^h + v_{0\mu}\frac{\tau_{0\mu}}{\tau_{1\mu}^h}\right]\nabla_{\mathbf{r}} c_h \qquad D_\mu = \frac{v_{0\mu}^2}{d\tau_{0\mu}^{-1}} + D_{t\mu} \tag{4.4}$$

which again can be written in terms of strain mobility and out-of-equilibrium chemical potential:

$$\partial_t \rho_\mu = \nabla_{\mathbf{r}} \cdot \left[M_\mu \nabla_{\mathbf{r}} \mathfrak{u}_\mu + \sqrt{2M_\mu}\mathbf{\Lambda}_\mu\right] \tag{4.5}$$

$$M_\mu(\mathbf{r}, [\{\rho_\mu\}]) = D_\mu(\mathbf{r}, [\{\rho_\mu\}])\rho_\mu(\mathbf{r}) \tag{4.6}$$

$$\mathfrak{u}_\mu(\mathbf{r}, [\{\rho_\nu\}]) = \log\rho_\mu(\mathbf{r}) + \frac{1}{2}\log D_\mu(\mathbf{r}, [\{\rho_\nu\}]) + \sum_{h=1}^{H}\underbrace{\left(v_{1\mu}^h + v_{0\mu}\frac{\tau_{0\mu}}{\tau_{1\mu}^h}\right)\frac{1}{dD_\mu(\mathbf{r}, [\{\rho_\nu\}])}}_{k_{\mu h}} c_h(\mathbf{r}, [\{\rho_\nu\}]) \tag{4.7}$$

where we have defined the coefficients $k_{\mu h}$.

4.2 Quorum Sensing

Our study on chemotaxis builds upon and extends the framework introduced in [6], which focuses on quorum sensing. We briefly review their main results here. The model therein considers S strains of run-and-tumble particles (RTPs), each with a self-propulsion speed regulated by S chemical fields according to:

$$v_\mu(\mathbf{r}_i, [\{\rho_\nu\}]) = v_0 \exp\left[\tanh\left(\sum_{\nu=1}^{S}\kappa_{\mu\nu}\frac{c_\nu(\mathbf{r}_i) - \bar{\rho}}{\varphi}\right)\right] \qquad c_\mu(\mathbf{r}) = (K * \rho_\mu)(\mathbf{r}) \tag{4.8}$$

where $\kappa_{\mu\nu}$ is a random Gaussian matrix with independent entries modeling weak, random interactions between strains:

$$\langle\kappa_{\mu\nu}\rangle = \frac{m}{S} \qquad \mathrm{Var}[\kappa_{\mu\nu}] = \frac{\sigma^2}{S} \tag{4.9}$$

with $m, \sigma^2 \sim \mathcal{O}(1)$. Numerical simulations show that increasing the heterogeneity σ^2 leads to a phase transition from a homogeneous to a fragmented ecosystem, where strains self-organize into distinct communities. This transition occurs both in the absence and in the presence of average motility inhibition—*i.e*, for $m = 0$ and $m < 0$, respectively.

Linear stability analysis of the coarse-grained hydrodynamic equation 4.5 around a homogeneous state $\boldsymbol{\rho}_0 \equiv \rho_0(1, \ldots, 1)$ can predict the emergence of such phases. The dynamics of a perturbation $\delta\hat{\rho}_\mu(\mathbf{q})$ in Fourier space is governed, to linear order, by:

$$\partial_t \delta\hat{\rho}_\mu(\mathbf{q}) = -\mathbf{q}^2 \mathcal{D}_{\mu\nu}\delta\hat{\rho}_\nu(\mathbf{q}) \,, \tag{4.10}$$

where $\mathbf{q}$ is the wavevector and $\mathcal{D}_{\mu\nu}$ is a diffusivity matrix depending on the couplings $\kappa_{\mu\nu}$. Instability arises when $\mathcal{D}$ has eigenvalues λ_i with negative real parts; in particular, the condition $\mathrm{Re}(\lambda_0) < 0$ for the eigenvalue λ_0 with smallest real part marks the onset of phase separation. Considering the case $\rho_0 = \bar{\rho}$, leads to the simplified diffusivity matrix:

$$\mathcal{D}_{\mu\nu} = \mathcal{D}_0\left(\delta_{\mu\nu} + \frac{\bar{\rho}}{\varphi}\kappa_{\mu\nu}\right) \quad \Rightarrow \quad \lambda_i = \mathcal{D}_0\left(1 + \frac{\bar{\rho}}{\varphi}\tilde{\lambda}_i\right) \tag{4.11}$$

where $\{\tilde{\lambda}_i\}$ are the eigenvalues of the matrix $\kappa_{\mu\nu}$. Results from random matrix theory are then used to compute the spectral properties of $\mathcal{D}$ in the limit of large S, allowing one to predict the location of the phase transition and the nature of the emerging fragmented state based on the eigenvectors associated to negative eigenvalues.

These predictions demonstrate that even weak ($\mathrm{Var}[\kappa_{\mu\nu}] \xrightarrow{S\to\infty} 0$), random motility regulation suffices to drive ecosystem fragmentation.

4.3 Chemotaxis

We devote the rest of the chapter to the original study of high-dimensional chemotaxis. We start with the most general setting allowing for H chemical fields, each of which can be produced by any strain ν:

$$c_h(\mathbf{r}, [\{\rho_\nu\}]) = \sum_{\nu=1}^{S} (K_{\nu h} * \rho_\nu)(\mathbf{r}) \tag{4.12}$$

We begin by carrying out the linear stability analysis of the fluctuating hydrodynamic equation 4.5. Taking the statistical average over the noise and applying a mean-field approximation yields:

$$\partial_t \langle \rho_\mu \rangle = \nabla \cdot [D_\mu \langle \rho_\mu \nabla \mathfrak{u}_\mu \rangle \approx \nabla \cdot [D_\mu \langle \rho_\mu \rangle \nabla \mathfrak{u}_\mu [\{\langle \rho_\nu \rangle\}] \tag{4.13}$$

We are interested in determining the stability of a homogeneous steady density profile $\boldsymbol{\rho} \doteq (\rho_1, \dots, \rho_S) = \boldsymbol{\rho}_0 = \rho_0(1, \dots, 1)$, which is the trivial solution. We consider then a small perturbation $\delta\boldsymbol{\rho}(\mathbf{r}, t)$ and expand the dynamics up to linear terms. From this point on, we omit the average brackets $\langle\rangle$.

$$\partial_t \delta\rho_\mu(\mathbf{r}, t) = \nabla \cdot \left\{ D_\mu \nabla \left[\delta\rho_\mu(\mathbf{r}, t) + \rho_0 \sum_h k_{\mu h} \sum_\nu (K_{\nu h} * \delta\rho_\nu)(\mathbf{r}, t) \right] \right\} + \mathcal{O}(\delta\boldsymbol{\rho}^2) \tag{4.14}$$

Taking the Fourier transform, we obtain:

$$\partial_t \delta\hat{\rho}_\mu(\mathbf{q}, t) = -\mathbf{q}^2 \sum_\nu \boldsymbol{M}_{\mu\nu}(\mathbf{q}) \delta\hat{\rho}_\nu(\mathbf{q}, t) \qquad \text{with} \qquad \boldsymbol{M}_{\mu\nu}(\mathbf{q}) = D_\mu \left(\delta_{\mu\nu} + \rho_0 \sum_h k_{\mu h} \hat{K}_{\nu h}(\mathbf{q}) \right) \tag{4.15}$$

where $\hat{K}_{\nu h}(\mathbf{q}) = \int d\mathbf{r} e^{-i\mathbf{q}\cdot\mathbf{r}} K_{\nu h}(\mathbf{r})$ is the Fourier transform of the coarse-graining kernel.

The homogeneous state becomes unstable when there exist a $\mathbf{q}$ for which the matrix $\boldsymbol{M}(\mathbf{q})$ has an eigenvalue λ_0 with negative real part. In order to progress further analytically we make some simplifying assumptions. First, we assume all strains have the same diffusivity, $D_\mu = D_0$, which is the case, for example, if they share the same mobility parameters v_0 and τ_0 in the absence of chemotactic regulation. Second, we assume the kernels have a common shape in $\mathbf{q}$, differing only by a strain-dependent amplitude: $\hat{K}_{\nu h}(\mathbf{q}) = \beta_{\nu h} \hat{K}(\mathbf{q})$. Under this assumptions:

$$\boldsymbol{M}_{\mu\nu}(\mathbf{q}) = D_0 \Big(\delta_{\mu\nu} + \rho_0 \hat{K}(\mathbf{q}) \underbrace{\sum_h k_{\mu h} \beta_{\nu h}}_{\alpha_{\mu\nu}} \Big) \qquad \Rightarrow \qquad \lambda_i(\mathbf{q}) = D_0 \left(1 + \rho_0 \hat{K}(\mathbf{q}) \tilde{\lambda}_i \right) \tag{4.16}$$

We define the matrix $\alpha_{\mu\nu} = \sum_h k_{\mu h}\beta_{\nu h}$, that quantifies how strain ν affects the motility of strain μ, summing over all the metabolic pathways connecting the two species. As discussed earlier, we take it to be symmetric, $\alpha_{\mu\nu} = \alpha_{\nu\mu}$, which, together with the fact that $\hat{K}(\mathbf{q}) \in \mathbf{R}$ (see appendix 6.1 for a proof), ensures real eigenvalues λ. Clearly, the matrices $\mathbf{M}_{\mu\nu}$ and $\alpha_{\mu\nu}$ share the same eigenvectors. The instability condition $\exists\mathbf{q}$ s.t. $\lambda_i(\mathbf{q}) < 0$ translates to:

$$\min_{\mathbf{q},i}\left[\hat{K}(\mathbf{q})\tilde{\lambda}_i\right] < -\frac{1}{\rho_0} \tag{4.17}$$

$$\min\left\{\tilde{\lambda}_{min}\max_{\mathbf{q}}\hat{K}(\mathbf{q}), \tilde{\lambda}_{max}\min_{\mathbf{q}}\hat{K}(\mathbf{q})\right\} < -\frac{1}{\rho_0} \tag{4.18}$$

If the kernel is positive in fourier space $\forall\mathbf{q}$[1], and since the r.h.s. is negative, the condition can only be satisfied if:

$$\tilde{\lambda}_{min}\max_{\mathbf{q}}\hat{K}(\mathbf{q}) < -\frac{1}{\rho_0} \tag{4.19}$$

As we have mentioned earlier, physically plausible kernels additionally respect $K(\mathbf{r}) > 0\ \forall\mathbf{r}$, which, as we show in the appendix 6.1, leads to $|\hat{K}(\mathbf{q})| \leq \hat{K}(0)$. The condition reduces then to the simpler:

$$\tilde{\lambda}_{min} < -\frac{1}{\rho_0\hat{K}(0)} \tag{4.20}$$

As discussed earlier, we model $\alpha_{\mu\nu}$ entries as Gaussian random variables with:

$$\langle\alpha_{\mu\nu}\rangle = \frac{m}{S} \qquad \mathrm{Var}[\alpha_{\mu\nu}] = \frac{\sigma^2}{S} \tag{4.21}$$

In the following, we will distinguish two regimes: absence of systematic motility regulation, given by $m = 0$, or cross motility inhibition between species, given by $m < 0$. As we will show, in the motility enhancement case $m > 0$ the phase diagram in unchanged with respect to $m = 0$.

In the absence of systematic regulation and in the limit of large S, the eigenvalues $\tilde{\lambda}$ follow a Wigner semi-circular law with support $[-2\sigma, 2\sigma]$, and the lowest eigenvalue is therefore $\tilde{\lambda}_{min} = -2\sigma$. It can be proven with tools from Random Matrix Theory that the corresponding eigenvectors have uniform distribution in the unit sphere $\mathbb{S}^S$, therefore, the eigenvector associated to the lowest eigenvalue $\tilde{\lambda}_{min}$ with be orthogonal to $(1, \ldots, 1)$, *i.e.* the dominant perturbation will have $\sum_\mu \delta\rho_\mu = 0$. This means that the corresponding density profile will be fragmented, featuring regions with high concentration of certain species and low of others.

[1]Note that the Fourier transform $\hat{K}(\mathbf{q})$ of the kernels that we used throughout this report is generally positive $\forall\mathbf{q}$: this condition is always true for the bell-shaped kernel of Equation 3.4 and also stands for the double exponential kernel defined in 3.9 when $\varepsilon < 1$, which is the interesting regime in which phase separation can occur.

When instead there is a nonzero average regulation ($m \neq 0$), the distribution of the eigenvalues $\tilde{\lambda}$ features the usual Wigner semicircle plus an isolated eigenvalue at $\lambda = m + \frac{\sigma^2}{m}$. When $\sigma < |m|$, this outlier is separated from the bulk of the distribution and is the smallest eigenvalue. In [1] it has been shown that the corresponding eigenvector $\delta\rho_\mu$ has $\sum_\mu \delta\rho_\mu = \sigma/|m|$, meaning that the perturbed density profile undergoes partial demixing: is well-mixed, or gregarious, for $\sigma = 0$, fragmentation then increases with σ until a maximum is reached at $\sigma = |m|$. Indeed, if $\sigma < |m|$, the outlier eigenvalue lies again within the bulk, and the lowest eigenvalue is again the lower end of the semicircle $\tilde{\lambda}_{min} = -2\sigma$ with the same eigenvector as before.

To summarize, instability arises when:

$$\begin{cases} \sigma^2 > \frac{1}{4\hat{K}^2(0)\rho_0^2} & \text{if } m = 0 \text{ or } \sigma^2 > m^2 \\ \sigma^2 > -\frac{m}{\hat{K}(0)\rho_0} - m^2 & \text{otherwise} \end{cases} \tag{4.22}$$

It can be checked by direct calculation that the phase-separating line is continuous and differentiable even when $m < 0$.

Figure 4.1 shows the phase diagram of the polydisperse system in presence and absence of systematic motility regulation.

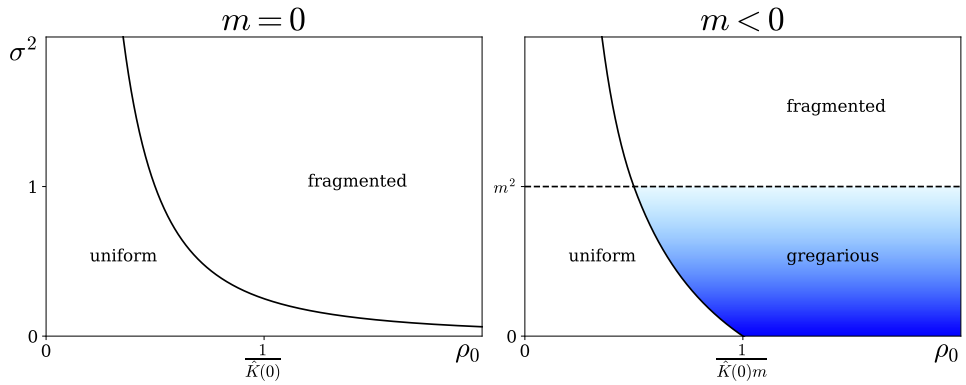

Figure 4.1: Phase diagram in the plane (σ^2, ρ_0) of the polydisperse system. In absence of average motility regulation ($m = 0$, left) the uniform density profile is stable for low values of the heterogeneity σ^2, then increasing this parameter above a critical line leads to fragmentation of the ecosystem and spatial demixing of species. When average interactions are motility inhibitory ($m < 0$, right) there is an additional gregarious phase, corresponding to phase separation with equal density distribution for every species, at $\sigma = 0$, or only partial demixing for $0 < \sigma^2 < |m|$. The color gradient quantifies the degree of fragmentation.

Chapter 5

Conclusions

In this work, we have explored how motility regulation drives self-organization in dry scalar active matter, both in monodisperse systems and in mixtures of many interacting species. Starting from microscopic models of active particles, we presented the coarse-graining procedure used to derive the macroscopic dynamics of the density field under both quorum sensing and chemotactic interactions. We revised the analytical methods used to characterize the onset of motility-induced phase separation (MIPS) in quorum sensing systems, and extended them to chemotactic interactions by deriving instability criteria from a hydrodynamic description and, where possible, constructing effective free energy functionals. For monodisperse systems, we validated our theoretical predictions through microscopic simulations in one spatial dimension, confirming the emergence of distinct regimes including homogeneous states, liquid-gas phase coexistence, and condensation, depending on the type and strength of interactions.

Numerics in $1d$, however, have proven to be problematic for accurately measuring the densities of the coexisting phases, due to the absence of long-range correlations in one-dimensional systems. Therefore, two-dimensional simulations have been developed to overcome this limitation. The predicting power of the theoretical methods employed-common tangent construction on a local approximation of free energy density, and linear stability analysis of the mean-field hydrodynamic equation-has proven limited in the case of composite chemotactic interactions. While both approaches correctly predict the onset of thermodynamic collapse for sufficiently strong attractive interactions, neither is able to capture the phase-separated regime or quantitatively predict the binodal densities. In future work, it would be interesting to go beyond the local approximation and develop non-local methods for constructing effective free energy landscapes, in order to better characterize phase coexistence in systems with competing attractive and repulsive chemotactic interactions.

We then extended the theoretical analysis to mixtures of multiple interacting strains, introducing random couplings to model weak, unspecific chemotactic cross-regulation. By applying linear stability analysis and tools from random matrix theory, we demonstrated that even these weak interactions can destabilize the homogeneous state, leading to the formation of fragmented, spatially structured communities. In the future, simulations of the high-dimensional system will be necessary to test and validate the original theoretical predictions developed here.

Chapter 6

Appendices

6.1 Generalities about Fourier transform

In this paragraph, we show some results about Fourier transform that have been employed to perform the Linear Stability Analysis of the fluctuating hydrodynamic equation in section 4.3. We use the convention:

$$\hat{f}(\mathbf{q}) = \int d\mathbf{r} e^{-i\mathbf{q}\cdot\mathbf{r}} f(\mathbf{r})$$
$$f(\mathbf{r}) = \frac{1}{2\pi} \int d\mathbf{q} e^{i\mathbf{q}\cdot\mathbf{r}} \hat{f}(\mathbf{q})$$

First, we note that in the context of this report, the kernel $K(\mathbf{r})$ defines the concentration of the chemical in space. Since the latter is, by definition, positive everywhere and for any distribution of the density ρ that produces it, the convoluting Kernel must also be everywhere positive in real space:

$$c(\mathbf{r}) = (K * \rho)(\mathbf{r}) > 0 \quad \forall \mathbf{r} \quad \forall \rho(\mathbf{r}) \qquad \Rightarrow \qquad K(\mathbf{r}) > 0 \quad \forall \mathbf{r}$$

This can be simply proven by taking $\rho(\mathbf{r}') = \delta(\mathbf{r}')$, leading to $K(\mathbf{r}') > 0$. Given the arbitrariness of the point $\mathbf{r}'$, the result follows straightforwardly.

In the report we have made use of the fact that $\hat{K}(\mathbf{q})$ is real $\forall \mathbf{q}$. This simply follows from the symmetry of the function in real space. Indeed, if $K(-\mathbf{r}) = K^*(\mathbf{r})$:

$$\begin{aligned}
\hat{K}^*(\mathbf{q}) &= \int d\mathbf{r} e^{i\mathbf{q}\cdot\mathbf{r}} K^*(\mathbf{r}) \\
&= \int d\mathbf{r} e^{-i\mathbf{q}\cdot(-\mathbf{r})} K(-\mathbf{r}) \\
&= \int d\mathbf{r} e^{-i\mathbf{q}\cdot\mathbf{r}} K(\mathbf{r}) \\
&= \hat{K}(\mathbf{q})
\end{aligned}$$

Now we can show that $|\hat{K}(\mathbf{q})| \leq \hat{K}(0)$:

$$\begin{aligned}
|\hat{K}(\mathbf{q})| &= \left| \int d\mathbf{r} e^{-i\mathbf{q}\cdot\mathbf{r}} K(\mathbf{r}) \right| \\
&\leq \int d\mathbf{r} \left| e^{-i\mathbf{q}\cdot\mathbf{r}} K(\mathbf{r}) \right| \\
&= \int d\mathbf{r} \left| e^{-i\mathbf{q}\cdot\mathbf{r}} \right| K(\mathbf{r}) \\
&= \hat{K}(0)
\end{aligned}$$

where we have used the positivity of $K(\mathbf{r})$ between the second and third line.

6.1.1 Bidimensional Fourier transform of K_0

In the following we detail the derivation of the bidimensional Fourier transform of the function $G(\mathbf{r}) = K_0(a|\mathbf{r}|)$ where we denote with $K_0(r)$ the 0^{th} order modified Bessel function of the second kind.

$$\hat{G}(\mathbf{q}) = \int d\mathbf{r}\ e^{-i\mathbf{q}\cdot\mathbf{r}} G(\mathbf{r}) \tag{6.1}$$

$$= \int_0^\infty dr \int_0^{2\pi} d\phi\ r\ e^{-iqr\cos\phi} G(r) \tag{6.2}$$

$$= 2\pi \int_0^\infty dr\ r J_0(qr) G(r) \tag{6.3}$$

$$= 2\pi \mathscr{H}_0 \left[G(r) \right](q) \tag{6.4}$$

$$\tag{6.5}$$

where we have defined the 0^{th} order Hankel transform $\mathscr{H}_0$ and in going from line 1 to 2 we have expanded in polar coordinates and implicitly set the zero of ϕ when $\mathbf{r}$ is aligned to $\mathbf{q}$, which was made possible by the circular symmetry of $G(\mathbf{r})$. K_0 belongs to a tabulated pair of known Hankel pairs (the Hankel transform is self-inverse), leading to:

$$\hat{G}(\mathbf{q}) = \frac{2\pi}{a^2 + |\mathbf{q}|^2} \tag{6.6}$$

Bibliography

[1] Florent Benaych-Georges and Raj Rao Nadakuditi. The eigenvalues and eigenvectors of finite, low rank perturbations of large random matrices. 2010.

[2] Howard C. Berg and Douglas A. Brown. Chemotaxis in escherichia coli analysed by three-dimensional tracking. *Nature*, 239:500–504, 1972.

[3] Elena O. Budrene and Howard C. Berg. Dynamics of formation of symmetrical patterns by chemotactic bacteria. *Nature*, 376(6535):49–53, 1995.

[4] Tobias Bäuerle, Andreas Fischer, Thomas Speck, and Clemens Bechinger. Self-organization of active particles by quorum sensing rules. *Nature Communications*, 9(1):3232, 2018.

[5] David S Dean. Langevin equation for the density of a system of interacting langevin processes. *Journal of Physics A: Mathematical and General*, 29(24):L613, dec 1996.

[6] Alberto Dinelli, Ada Altieri, and Julien Tailleur. Random motility regulation drives the fragmentation of microbial ecosystems. 2025.

[7] Alberto Dinelli, Jérémy O'Byrne, and Julien Tailleur. Fluctuating hydrodynamics of active particles interacting via taxis and quorum sensing: static and dynamics. *Journal of Physics A: Mathematical and Theoretical*, 57(39):395002, sep 2024.

[8] M Ester, H P Kriegel, J Sander, and Xu Xiaowei. A density-based algorithm for discovering clusters in large spatial databases with noise. AAAI Press, Menlo Park, CA (United States), 12 1996.

[9] François A. Lavergne, Hugo Wendehenne, Tobias Bäuerle, and Clemens Bechinger. Group formation and cohesion of active particles with visual perception–dependent motility. *Science*, 364(6435):70–74, 2019.

[10] C. Liu, X. Fu, L. Liu, X. Ren, C. K. Chau, S. Li, L. Xiang, H. Zeng, G. Chen, L. H. Tang, P. Lenz, X. Cui, W. Huang, T. Hwa, and J. D. Huang. Sequential establishment of stripe patterns in an expanding cell population. *Science*, 334(6053):238–241, Oct 2011.

[11] J. O'Byrne and J. Tailleur. Lamellar to micellar phases and beyond: When tactic active systems admit free energy functionals. *Phys. Rev. Lett.*, 125:208003, Nov 2020.

[12] Jérémy O'Byrne, Alexandre Solon, Julien Tailleur, and Yongfeng Zhao. An introduction to motility-induced phase separation. In *Out-of-equilibrium Soft Matter*. The Royal Society of Chemistry, 03 2023.

[13] Alexandre P. Solon, Michael E. Cates, and Julien Tailleur. Active brownian particles and run-and-tumble particles: A comparative study. *The European Physical Journal Special Topics*, 224(7):1231–1262, 2015.

[14] Alexandre P. Solon, Joakim Stenhammar, Michael E. Cates, Yariv Kafri, and Julien Tailleur. Generalized thermodynamics of phase equilibria in scalar active matter. *Phys. Rev. E*, 97:020602, Feb 2018.